

UNIVERSITY OF EXETER

# Transport Properties of Graphene Doped with Adatoms

by

James McMurray

Collaborators: Chris Beckerleg and Will Smith

Supervisor: Dr. A. Shytov

April 2013



## ABSTRACT

A numerical model of electron transport in monolayer graphene was produced, and the effects of doping and the application of magnetic field were analysed. It was found that the states near zero energy appear to be delocalised. The zeroth Landau level in graphene was found to require a critical magnetic field for conduction at low energies, while high magnetic fields also resulted in localised states. The floating up of Landau levels was also observed at low magnetic fields as predicted by Khmelnitskii[1]. Possibilities for future work are also suggested, such as an investigation of the effects of varying the vacancy concentration.



# Contents

<b>1</b>	<b>Introduction</b>	<b>1</b>
<b>2</b>	<b>Background Theory</b>	<b>3</b>
2.1	The lattice structure of graphene . . . . .	3
2.2	The Tight Binding approximation . . . . .	4
2.3	Dirac points and the linear dispersion relation . . . . .	5
2.4	Density of states . . . . .	8
2.5	The Klein Effect . . . . .	9
2.6	The Landauer Formula . . . . .	11
2.7	The Quantum Hall Effect . . . . .	11
2.8	Localisation . . . . .	13
<b>3</b>	<b>Method and Implementation</b>	<b>15</b>
3.1	Representation of the graphene sample . . . . .	15
3.2	Scattering Matrix approach overview . . . . .	16
3.2.1	Generation of $M$ matrix . . . . .	17
3.2.2	Updating transmission matrices . . . . .	18
3.3	Tests of correctness . . . . .	19
3.3.1	Unitarity checking . . . . .	19
3.3.2	Analytical tests . . . . .	20
3.4	Implementation of magnetic field . . . . .	23
3.5	Implementation of disorder . . . . .	25
<b>4</b>	<b>Results</b>	<b>27</b>
4.1	Size effects . . . . .	28
4.2	Zero energy conductance peak . . . . .	29
4.3	Localisation length . . . . .	30
4.4	Phase diagrams . . . . .	31
4.5	Comparison with current experimental capabilities . . . . .	32
<b>5</b>	<b>Conclusion</b>	<b>35</b>
5.1	Summary . . . . .	35
5.2	Future work . . . . .	35
<b>A</b>	<b>Flowchart</b>	<b>37</b>
<b>B</b>	<b>Source code excerpts</b>	<b>39</b>
B.1	Analytical ladder test program . . . . .	39

B.2 Allocation of random vacancy sites . . . . .	40
<b>Bibliography</b>	<b>43</b>

# List of Figures

2.1	A diagram of the real space lattice of graphene. Note the two sublattices A and B. . . . .	3
2.2	Labelling the sites 1-4. . . . .	4
2.3	A diagram of the band structure of graphene. The Dirac points are where the bands converge (zoomed on the right). Adapted from [11]. . . . .	6
2.4	A diagram of the first Brillouin zone in reciprocal space. The unique Dirac points are $K$ and $K'$ , $M$ is the midpoint and $\Gamma$ is the symmetry point shown as convention. . . . .	6
2.5	A plot of the density of states for a $50 \times 86$ sample with 3% vacancy concentration on the A and B sublattices and 50 randomisations. . . . .	9
2.6	A plot of the transmission probability, $T$ , as a function of the angle of incidence, $\phi$ , for a potential of 285 meV (solid line) and 200meV (dashed line). Adapted from [5]. . . . .	10
2.7	A diagram showing the principle of how the transmission occurs across a potential barrier of height $V$ , by shifting the electron to the lower cone. The filled area represents the portion filled with electrons. Note the constant Fermi level in the conduction band outside the barrier, and in the valence band within it. Adapted from [5]. . . . .	10
2.8	A theoretical graph of the Hall conductivity (right axis, plateaus line) and longitudinal resistivity (left axis, peaks line) in monolayer graphene. Note the half-integer values of the Hall-conductivity and the peaks of the longitudinal resistivity at the plateau steps. Adapted from [19]. . . . .	13
3.1	A diagram showing how the original graphene lattice structure is considered as a “brick-wall” to simplify the links between lattice points. The dashed lines separate the slices across which the transmission matrices are calculated and updated consecutively (this diagram shows the case for conduction in the X direction). . . . .	16
3.2	A diagram of an example lattice to how the simultaneous equations are constructed, in this case demonstrating the case of X-directed current. The different groups of sites are marked in different colours. . . . .	17
3.3	A diagram showing the net transmission across two blocks. One must include the contributions from all of the possible paths, resulting in a geometric sum. . . . .	19
3.4	A diagram of the “ladder” configuration for which the analytical tests were derived. . . . .	20

3.5	A plot of the results of the analytical equations against the program output for a $2 \times 4$ lattice, with conduction in the Y-direction as shown in Figure 3.4. The squares of the transmission values are plotted against the energy. The circles are the program output, and the lines are the analytical results. Note there are two T values since the (horizontal) width is 2. The net conductance is simply the sum of the transmission values. . . . .	23
3.6	A plot of the quantum Hall steps in the wrapped and unwrapped conductance for a $160 \times 277$ sample, with the current in the X-direction and magnetic vector potential in the Y-direction, at a flux of 0.0227. The wrapped conductance is appropriately modified so it can be viewed on the same scale. The theoretical values of the QHE steps are shown with dotted lines. . . . .	25
4.1	Conductance for various sizes of square samples, showing the transition from the delocalised to the localised regime near $E = \pm 0.2$ . . . . .	28
4.2	A zoomed plot of the central, low energy region of Figure 4.1 showing the conductance peak at $E = -10^{-3}$ . . . . .	29
4.3	A plot of the localisation length against energy. . . . .	30
4.4	Wrapped sample with the theoretical position of the 1st, 2nd and 3rd Landau level plotted in the dashed white lines, see Equation (2.30). The sample size was $100 \times 174$ , with X wrapping enabled, 1.5% vacancy concentration on the A and B sublattices and 20 randomisations. . . . .	31
4.5	A zoom of Figure 4.4 at low energy, showing delocalised states produced by the applied magnetic field. The sample size was $100 \times 174$ , with X wrapping enabled, 1.5% vacancy concentration on the A and B sublattices and 50 randomisations. . . . .	32



# Chapter 1

## Introduction

Graphene is an allotrope of carbon consisting of carbon atoms in a two-dimensional, bipartite lattice consisting of two interpenetrating triangular sublattices. Graphene was first isolated in 2004 by Geim, Novoselov and their colleagues[2], and was the first 2D crystal to be successfully isolated. They demonstrated its interesting electronic properties and, since then, interest in graphene has flourished.

In their initial work, Geim *et al.* isolated graphene through the micromechanical exfoliation of graphite. Sticky tape was used to repeatedly peel layers of carbon atoms from a graphite sample until only a single layer remained on the sticky tape. The carbon flakes were then transferred to a Silicon Dioxide substrate where the graphene flakes were detected with an optical microscope due to the interference they produce when on the substrate[3]. However, new methods of isolation for mass production, such as Chemical Vapour Deposition, are now being pursued[4]. This means that understanding graphene's electrical properties is an urgent and vital research effort.

Graphene has a remarkable number of theoretically interesting phenomena. The quasi-particles act as massless Dirac fermions near the Dirac points, and so demonstrate relativistic behaviour, such as the unintuitive Klein Paradox[5]. The suppression of localisation also leads to the apparent universal minimum conductivity (the so-called “conductivity without charge carriers”[6]), meanwhile the origin of the missing Pi problem, where the experimental value of the minimum conductivity is observed to be an order of pi larger than the theoretical value, remains unclear[6].

Due to its unique electrical properties, graphene has a huge range of prospective applications from mass sensors[7], to photodetectors[8] and high frequency transistors[9]. However, graphene field effect transistors currently have low on-off ratios, meaning the transistors cannot be turned off effectively. This may be overcome by creating a band gap in the sample, for example, by doping with hydrogen to produce graphane[10]. Our theoretical investigation into the effects of magnetic field and doping in graphene is relevant to these practical problems.

Our work focussed on investigating the effects of doping and magnetic field on the conduction in monolayer graphene samples. A numerical model was developed using FORTRAN 77 and the LAPACK linear algebra package, so that the effects of magnetic field and vacancy concentration could be investigated.

## Chapter 2

# Background Theory

This chapter details several aspects of the background theory regarding graphene, which are relevant to the methods we have used and the analysis of our results.

### 2.1 The lattice structure of graphene

Graphene consists of carbon atoms in a hexagonal structure, as shown in Figure 2.1. However, this is not a Bravais lattice, but is a bipartite lattice consisting of two interpenetrating triangular sublattices, which are labelled A and B in the figure.

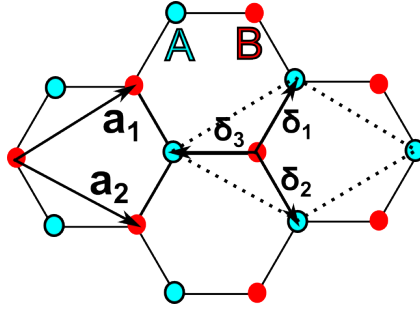


FIGURE 2.1: A diagram of the real space lattice of graphene. Note the two sublattices A and B.

The lattice vectors for the sublattices,  $\mathbf{a}_1$  and  $\mathbf{a}_2$ , can be written as:

$$\mathbf{a}_1 = \frac{3a}{2} \hat{\mathbf{i}} + \frac{\sqrt{3}a}{2} \hat{\mathbf{j}}, \quad \mathbf{a}_2 = \frac{3a}{2} \hat{\mathbf{i}} - \frac{\sqrt{3}a}{2} \hat{\mathbf{j}} \quad (2.1)$$

While the nearest-neighbour vectors,  $\vec{\delta}_1$ ,  $\vec{\delta}_2$  and  $\vec{\delta}_3$  are given by:

$$\vec{\delta}_1 = \frac{a}{2} \hat{\mathbf{i}} + \frac{a\sqrt{3}}{2} \hat{\mathbf{j}}, \quad \vec{\delta}_2 = \frac{a}{2} \hat{\mathbf{i}} - \frac{a\sqrt{3}}{2} \hat{\mathbf{j}}, \quad \vec{\delta}_3 = -a \hat{\mathbf{i}} \quad (2.2)$$

Where the carbon-carbon distance,  $a \approx 1.42\text{\AA}$  [11].

## 2.2 The Tight Binding approximation

The Tight Binding approximation assumes the electrons are tightly bound to their corresponding atoms, and so the electrons can only reside at lattice sites.

In this work, only nearest neighbour hopping is taken in to account, and so electrons can only move from a site on sublattice A to a site on sublattice B and vice versa. This is an acceptable approximation as the next nearest neighbour hopping energy is only approximately 3.5% of the value of the nearest neighbour hopping energy[11], and so there is no major loss of information for the additional simplicity.

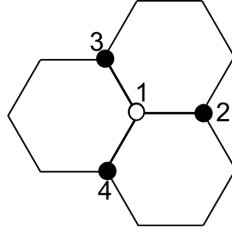


FIGURE 2.2: Labelling the sites 1-4.

In the Tight Binding model,  $H_{ij}$  i.e. the  $(i, j)_{\text{th}}$  element of the Hamiltonian is the energy cost of hopping from site  $i$  to site  $j$ . Considering only the sites labelled 1 to 4, as shown in Figure 2.2, the Hamiltonian can be written as shown in Equation (2.3), where  $t$  is the nearest neighbour hopping energy,  $t \approx 2.8\text{eV}$ [11], and  $E_i$  is the potential the  $i_{\text{th}}$  lattice point.

$$\hat{H} = \begin{pmatrix} E_0 & -t & -t & -t \\ -t & E_1 & 0 & 0 \\ -t & 0 & E_2 & 0 \\ -t & 0 & 0 & E_3 \end{pmatrix} \quad (2.3)$$

To obtain the energy eigenvalues of the system, the Time Independent Schrödinger Equation (TISE) is applied:

$$E\psi = \hat{H}\psi \quad (2.4)$$

Bloch theory states that the eigenfunction can be written as the product of a plane wave and a periodic function:

$$\psi_A = \tilde{\psi}_A e^{i(\mathbf{k} \cdot \mathbf{r})} \quad , \quad \psi_B = \tilde{\psi}_B e^{i(\mathbf{k} \cdot \mathbf{r})} \quad (2.5)$$

So by substituting Equation (2.5) in to Equation (2.4), with  $\mathbf{r}$  having its origin at point 1, the TISE can be written as:

$$E\tilde{\psi}_A = - \sum_{i,j} H_{ij}\psi_j = H_{12}\psi_2 + H_{13}\psi_3 + H_{14}\psi_4 = -t(\psi_2 + \psi_3 + \psi_4) \quad (2.6)$$

But  $\mathbf{k} \cdot \mathbf{r}$  in Equation (2.5) can be expressed as:

$$\mathbf{k} \cdot \mathbf{r} = k_x x + k_y y \quad (2.7)$$

By writing the wavefunctions in terms of Bloch waves (Equation (2.5)), substituting in the lattice vectors and wave vectors from Equation (2.7), and expressing the TISE in terms of the non-zero elements of the Hamiltonian (as in Equation (2.6)), the TISE can be written as:

$$\begin{aligned} E\tilde{\psi}_A &= -t\tilde{\psi}_B \left( \exp(ik_x a) + \exp\left(\frac{-ik_x a}{2} + \frac{ik_y a\sqrt{3}}{2}\right) + \exp\left(\frac{-ik_x a}{2} - \frac{ik_y a\sqrt{3}}{2}\right) \right) \\ &= -t(k)\tilde{\psi}_B \end{aligned} \quad (2.8)$$

Repeating the process for a point on sublattice B, and combining the equations obtains the complete expression for the TISE of the system:

$$E\psi = \begin{pmatrix} 0 & -\tilde{t}(k) \\ -\tilde{t}^*(k) & 0 \end{pmatrix} \psi \quad (2.9)$$

Taking the eigenvalues of this matrix obtains the energy eigenvalues of the system:

$$E = \pm |\tilde{t}(k)| \quad (2.10)$$

## 2.3 Dirac points and the linear dispersion relation

Figure 2.3 is a plot of the electronic band structure of graphene. The Dirac points are where the bands converge, their points in  $k$ -space given by the condition in Equation (2.11). In undoped graphene, the Fermi level lies across the Dirac points

$$|\tilde{t}(k)| = 0 \quad (2.11)$$

In reciprocal space, the Dirac points lie on the vertices of the first Brillouin Zone (i.e. the Wigner-Seitz cell of the reciprocal lattice) as shown in Figure 2.4.

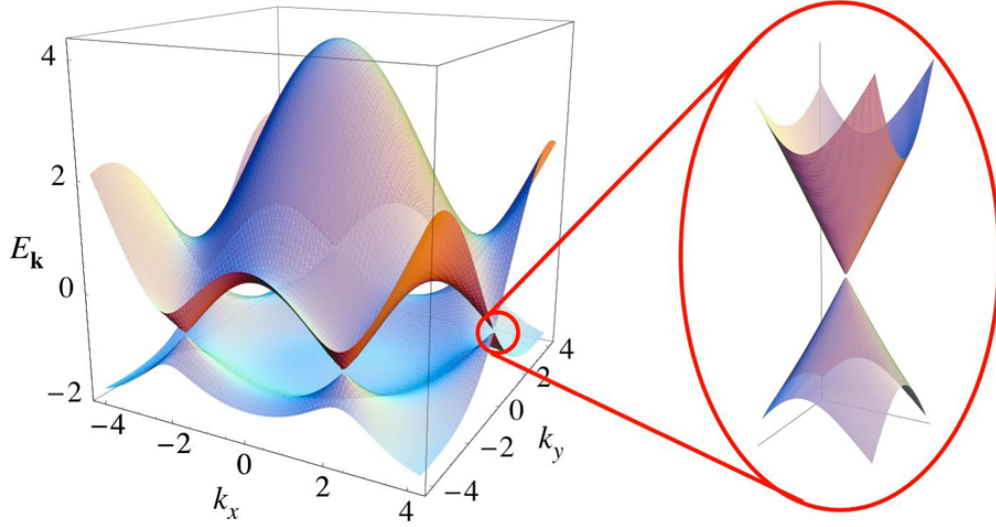


FIGURE 2.3: A diagram of the band structure of graphene. The Dirac points are where the bands converge (zoomed on the right). Adapted from [11].

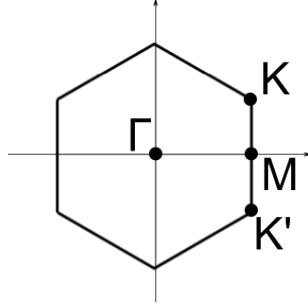


FIGURE 2.4: A diagram of the first Brillouin zone in reciprocal space. The unique Dirac points are  $K$  and  $K'$ ,  $M$  is the midpoint and  $\Gamma$  is the symmetry point shown as convention.

$K$  and  $K'$  are the unique Dirac points, as all of the other vertices can be expressed as equivalent to either of them. The co-ordinates of the Dirac points,  $K$  and  $K'$  are:

$$K = \left( \frac{2\pi}{3a}, \frac{2\pi}{3\sqrt{3}a} \right), \quad K' = \left( \frac{2\pi}{3a}, \frac{-2\pi}{3\sqrt{3}a} \right) \quad (2.12)$$

The Hamiltonian can be linearised near the Dirac points. From Equation (2.8), the expression for  $\tilde{t}(k)$  at the Dirac points can be written as:

$$|\tilde{t}(k)| = t \left| \exp(ik_x a) + \exp\left(\frac{-ik_x a}{2}\right) 2 \cos\left(\frac{k_y \sqrt{3}a}{2}\right) \right| = 0 \quad (2.13)$$

The Taylor approximation near  $K$  can then be written as: (2.14).

$$\tilde{t}(K + \delta k) \approx \tilde{t}(K) + \delta k_x \frac{\partial \tilde{t}(k)}{\partial k_x} + \delta k_y \frac{\partial \tilde{t}(k)}{\partial k_y} \quad (2.14)$$

Calculating the differentials, and substituting the expression for  $K$  from Equation (2.12),  $\tilde{t}(k)$  near  $K$  can be expressed as:

$$\tilde{t}(K + \delta k) \approx \frac{3at}{2}\delta k_x + \frac{3at}{2}\delta k_y \quad (2.15)$$

Substituting this in to Equation (2.9), yields the expression for the Hamiltonian near  $K$ :

$$H_K(k) = \frac{3at}{2} \begin{pmatrix} 0 & -k_y - ik_x \\ -k_y + ik_x & 0 \end{pmatrix} \quad (2.16)$$

This can be written in terms of the Pauli matrices by rotating the  $k$ -vector, so  $k_x$  is replaced with  $k_y$  and  $k_y$  is replaced with  $-k_x$ , producing the expression in Equation (2.17).

$$H_K(k) = \frac{3at}{2} \vec{\sigma} \cdot \vec{k} \quad (2.17)$$

By the same consideration, the expression for the Hamiltonian near  $K'$  in Equation (2.18) can be derived.

$$H_{K'}(k) = \frac{-3at}{2} \vec{\sigma}^* \cdot \vec{k} \quad (2.18)$$

Taking the eigenvalues of the Hamiltonian near  $K$  or  $K'$  obtains the linear dispersion relation:

$$\varepsilon = \frac{3at}{2} k = v\hbar k \quad (2.19)$$

The linear dispersion relation means the quasiparticles are massless Dirac fermions with constant velocity  $v$  (where  $v \approx 10^6 \text{ m s}^{-1}$ )[11]. This is relevant for the transport properties of graphene, as all quantum transport occurs near the Dirac points since the Fermi energy is low in comparison with the local peak energy (where the linear approximation breaks down) of  $t \approx 2.8\text{eV}$ [11], which corresponds to a Fermi temperature of approximately 30,000K.

The  $t$  values were determined from cyclotron resonance experiments, which provide experimental evidence for the linear dispersion relation in graphene[12].

It can also be shown that the density of states has a linear dependence with respect to energy near the Dirac point, using the dispersion relation. The area of each allowed

k-state is:

$$A_k = \left( \frac{2\pi}{a} \right)^2 \quad (2.20)$$

So considering a circle of area  $\pi k^2$  in reciprocal space, one obtains:

$$N(k) = \frac{4\pi k^2}{\left( \frac{2\pi}{a} \right)^2} = \frac{k^2 a^2}{\pi} = \frac{A k^2}{\pi} \quad (2.21)$$

Substituting the dispersion relation (Equation (2.19)) obtains:

$$N(E) = \frac{AE^2}{\pi v^2 \hbar^2} \quad (2.22)$$

And differentiating to obtain the density of states near the Dirac points:

$$g(E) = \frac{N(E)}{dE} = \frac{2AE}{\pi v^2 \hbar^2} \propto E \quad (2.23)$$

## 2.4 Density of states

In preliminary work we produced a plot of the density of states against energy. This was calculated by producing the Hamiltonian matrix for the sample (see Section 2.2 for details on the form of the Hamiltonian matrix), and then producing a histogram of the energy eigenvalues.

Figure 2.5 shows a plot of the density of states for a disordered sample, with equal numbers of vacancies on the A and B sublattices. The on-site vacancy potential,  $U_0$ , was set to 1000. Note the states available near zero energy which are not present in the case of a pure sample.

Our work is focused in the low-energy region, near the Dirac points where the density of states is approximately linear. The peaks at  $\pm 1 t$  are known as the Van Hove singularities, which occur at the edge of the Brillouin zone and are important for the optical properties of graphene[13]. However, this region is not the subject of our investigation.



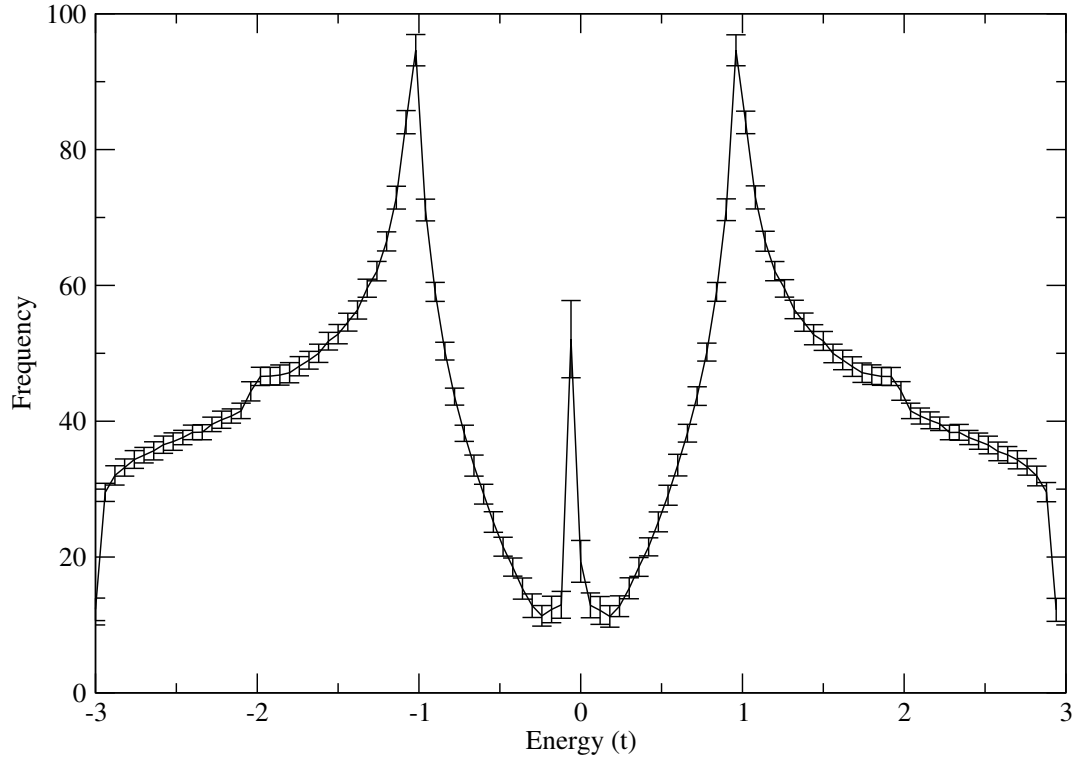


FIGURE 2.5: A plot of the density of states for a  $50 \times 86$  sample with 3% vacancy concentration on the A and B sublattices and 50 randomisations.

## 2.5 The Klein Effect

The Klein Effect is a consequence of the linear dispersion of the massless quasiparticles. It is the counterintuitive result that in the case of quantum tunneling across a potential barrier, the transmission probability increase with the height of the potential barrier, and tends to 1 as the potential tends to infinity[5]. It is this effect that makes undoped graphene difficult to use in electronic devices.

For high barriers ( $|V_0| \gg |E|$ ) the transmission probability,  $T$ , can be written as in Equation (2.24), where  $\phi$  is the angle of incidence,  $q_x$  is the x-component of the wavevector within the barrier and  $D$  is the width of the potential barrier[5].

$$T = \frac{\cos^2(\phi)}{1 - \cos^2(q_x D) \sin^2(\phi)} \quad (2.24)$$

Figure 2.6 is a plot of the transmission probability as a function of the angle of incidence. Note the broad peak at normal incidence.

Figure 2.7 shows how the transmission occurs for an electron. When tunneling through the barrier, the electron acts as a hole travelling in the opposite direction as they are on the same branch of the electronic spectrum (the diagonal line in the diagram), which

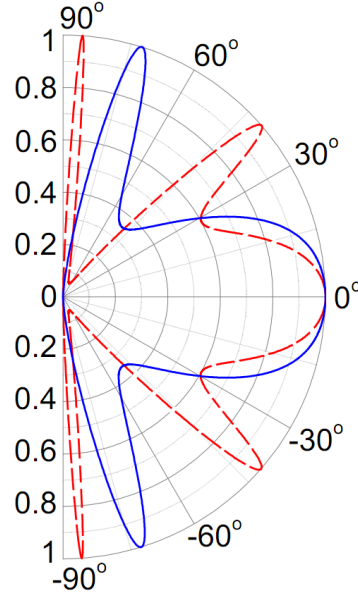


FIGURE 2.6: A plot of the transmission probability,  $T$ , as a function of the angle of incidence,  $\phi$ , for a potential of 285 meV (solid line) and 200meV (dashed line). Adapted from [5].

is an identical situation[5]. Note that this assumes there is no mixing of the  $K$  and  $K'$  cones, which would allow scattering on to the other cone, and so reflection rather than transmission[11].

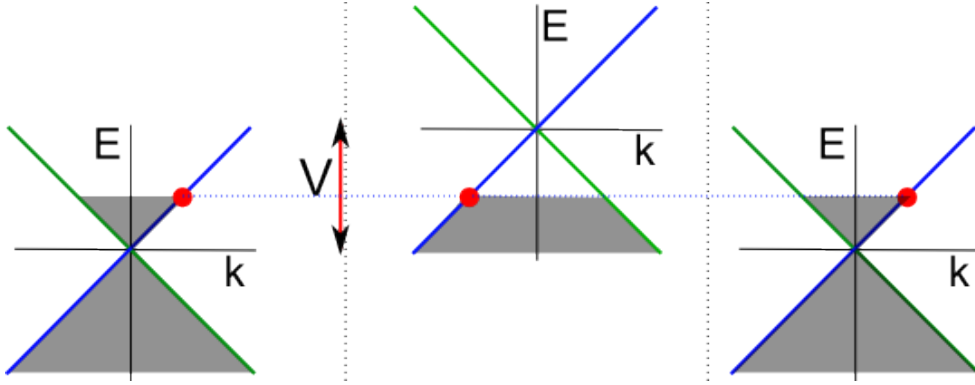


FIGURE 2.7: A diagram showing the principle of how the transmission occurs across a potential barrier of height  $V$ , by shifting the electron to the lower cone. The filled area represents the portion filled with electrons. Note the constant Fermi level in the conduction band outside the barrier, and in the valence band within it. Adapted from [5].

This has the result that the quasiparticles cannot be localised in undoped graphene, which leads to the phenomenon of universal minimum conductivity. Note that it does not occur for doped graphene, as there is a possibility of scattering on to the other Dirac cone which results in reflection of the quasiparticle from the barrier.

The Klein effect appears to have been experimentally observed in measurements of quantum conductance in narrow graphene structures[14]. This is the first observation

of the Klein effect.

## 2.6 The Landauer Formula

The Landauer Formula is used to calculate the conductance of the sample. The equation for the net conductance, Equation (2.25), is derived by considering the electrons that are able to move across a potential, with respect to the Fermi-Dirac distribution[15].  $G$  is the net conductance of the sample, and  $T_i$  is the transmission coefficient for the  $i_{th}$  channel to take in to account varying transmission coefficients.

$$G \approx \frac{e^2}{\pi\hbar} \sum_i T_i \quad (2.25)$$

The per channel conductivity is given in Equation (2.26). Note that there is no temperature dependence, and so this means there is a minimum conductivity even in undoped graphene at low temperatures when normal semiconductors become insulators[6]. This is a remarkable and unintuitive property of graphene when compared with other semiconductors.

$$\sigma \approx \frac{e^2}{\pi\hbar} \quad (2.26)$$

However, when the minimum conductivity was measured experimentally, it was found to be an order of  $\pi$  larger. This is known as the “Missing Pi Problem” and the exact reason for the discrepancy remains unknown[6]. However, experimental work by Miao *et al.* in 2007 reported that the experimental value of the minimum conductivity approached the theoretical value for small, wide rectangles of graphene, after testing various rectangles[16].

## 2.7 The Quantum Hall Effect

The quantum Hall effect is the phenomenon whereby the Hall conductivity is observed to be quantised in to a series of plateaus. In the standard integer quantum Hall effect, the Hall conductivity is given by Equation (2.27), where  $\sigma_{xy}$  is the Hall conductivity and  $\nu$  is the filling factor which is a non-zero integer in this integer case[17].

$$\sigma_{xy} = \nu \frac{e^2}{h} \quad (2.27)$$

Landau quantisation is the quantisation of the orbits of charged particles in a magnetic field. This results in Landau levels which are levels of constant energy consisting of many degenerate states[18]. The quantum Hall effect is observed under strong magnetic fields, when the number of degenerate states per Landau level is high. The equation for the number of degenerate states in a Landau level is given in Equation (2.28), where  $g_s$  is the spin degeneracy factor,  $B$  is the magnitude of the applied magnetic field,  $A$  is the area of the sample and  $\phi_0$  is the quantum of the magnetic flux[18].

$$N_d = \frac{g_s B A}{\phi_0} \quad (2.28)$$

The electrons fill up the Landau levels in order of increasing energy[18]. It is only at the transitions between Landau levels that the quantised energy of the cyclotron orbit changes, and so the Hall conductivity can increase, and so plateaus with steps are produced. The density of states peaks at the steps between Landau levels, whilst being zero elsewhere, and so the longitudinal resistivity peaks at these points. Disorder has the effect of broadening these peaks, eventually destroying the plateau structure at large disorder[18].

In graphene, the quantum Hall effect takes a “half-integer” form, so the plateaus have the expected step height but the sequence is shifted by a half[19]. The equation for the Hall conductivity then takes the form in Equation (2.29), where the factor of 4 occurs due to double spin degeneracy from the actual spin and pseudo-spin (describing the current sublattice of the electron)[19].

$$\sigma_{xy} = \frac{4e^2}{h} \left( \pm N + \frac{1}{2} \right) \quad (2.29)$$

The anomalous shift in the sequence of  $\sigma_{xy}$  plateaus in graphene is a result of the presence of the zero energy level, which draws half of its electrons from the valence band and half from the conduction band[3]. This state itself is a result of the linear dispersion relation of graphene in a magnetic field, which is described by Equation (2.30), where the  $\pm$  factor represents electrons and holes,  $N$  is an integer,  $B$  is the magnitude of the applied magnetic field and  $v_F$  is the constant velocity of the Dirac fermions[19].

$$E_N = \pm v_F \sqrt{2e\hbar B N} \quad (2.30)$$

A plot of the Hall conductivity in graphene calculated from theory is shown in Figure 2.8 (adapted from [19]). Note the half-integer values of the Hall conductivity at the plateaus, and how the longitudinal resistivity peaks at the steps between plateaus.

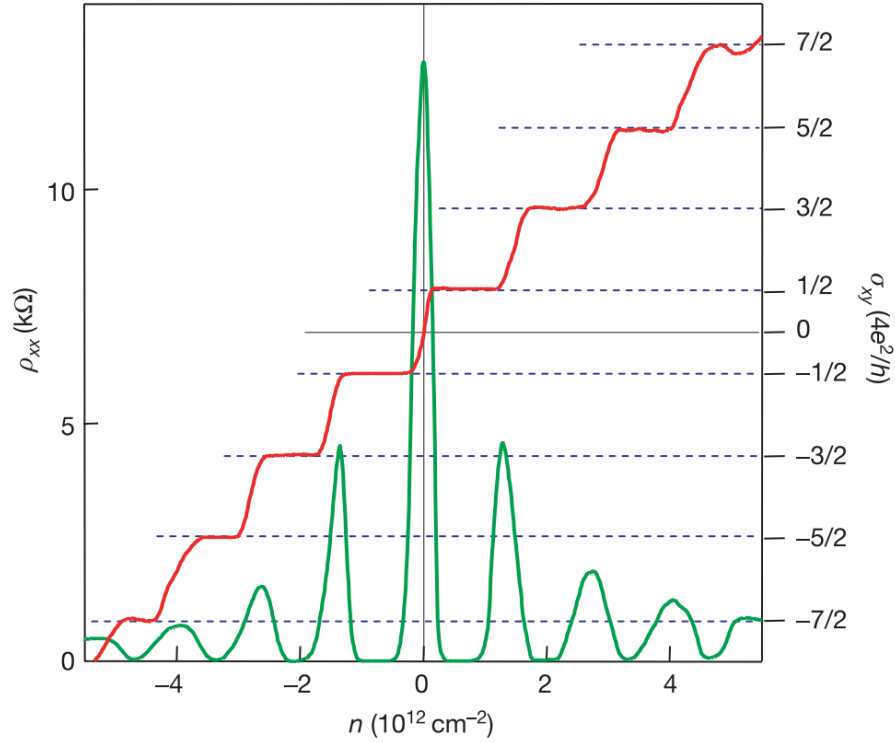


FIGURE 2.8: A theoretical graph of the Hall conductivity (right axis, plateaus line) and longitudinal resistivity (left axis, peaks line) in monolayer graphene. Note the half-integer values of the Hall-conductivity and the peaks of the longitudinal resistivity at the plateau steps. Adapted from [19].

## 2.8 Localisation

Localised states which are defined as the states whose wavefunctions are concentrated mainly in a confined region and exponentially decay outside of this region[20]. Localised electrons are confined to specific sites, and cannot contribute to the net conduction of the sample. In contrast, delocalised electrons can move through-out the sample, and so contribute to conduction.

The scaling theory of localisation models localisation by considering the dimensionless conductance as a function of scale variables, such as the system size,  $L$ . In the delocalised phase in a 2-dimensional system, the conductance is independent of system size[21].

$$g(L) \sim \sigma \quad (2.31)$$

Where  $\sigma$  is the conductivity of the sample.

In the localised phase, however, conduction occurs by tunneling between states of approximately equal energy. This results in an exponentially decaying behaviour for the conductance with respect to system size[21]:

$$g(L) \sim e^{\frac{-L}{\xi}} \quad (2.32)$$

Where  $L$  is the sample size, and  $\xi$  is the localisation length. Note that the limit of large localisation length ( $\xi \gg L$ ) tends towards the delocalised case.

## Chapter 3

# Method and Implementation

This chapter details the method which were used to develop the numerical model, and the specifics of the implementation. The model was written in FORTRAN 77 using the LAPACK linear algebra package for the matrix calculations. The source code is freely available on Github[22]. A simplified flowchart of the program’s operation is given in Appendix A.

A computational approach is necessary in order to model the disorder, as it allows a Monte Carlo approach to be used: producing and averaging many randomised disorder configurations. The computational time required to run the calculations is significant, even with some optimisations that were made, running 50 lattice randomisations over 100 energy values for a lattice size of  $100 \times 174$  requires about 12 hours, depending on the hardware. The slowest parts of the calculations are the matrix inversions and multiplications which are of order  $O(n^3)$ , so some efforts were made to split and reduce the size of the matrices where possible.

### 3.1 Representation of the graphene sample

In the model, the honeycomb lattice is translated to a “brick-wall” model, as shown in Figure 3.1, for the calculations. This means that to obtain a square lattice in real space, the vertical size must equal the horizontal size multiplied by  $\sqrt{3}$  due to the change in shape of the real lattice.

The transmission matrices are calculated across each slice consecutively, updating the net sample transmission matrices progressively. This was implemented as it is more efficient than solving the equations for a single, large net transfer matrix.

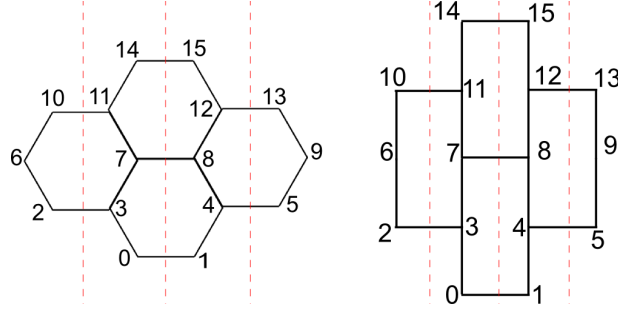


FIGURE 3.1: A diagram showing how the original graphene lattice structure is considered as a “brick-wall” to simplify the links between lattice points. The dashed lines separate the slices across which the transmission matrices are calculated and updated consecutively (this diagram shows the case for conduction in the X direction).

### 3.2 Scattering Matrix approach overview

The transfer matrix,  $M$ , expresses the equations between the slices in the matrix, as shown in Equation (3.1).

$$\begin{pmatrix} \psi_3 \\ \psi_4 \end{pmatrix} = M \begin{pmatrix} \psi_1 \\ \psi_2 \end{pmatrix} \quad (3.1)$$

These relations are defined by the application of the Time Independent Schrödinger Equation (Equation (2.4)) and the tight binding approximation. To obtain the transmission values, it is necessary to solve this system of simultaneous equations across the slice, doing this requires defining the  $O$  matrix through the consideration of left and right travelling waves.

$$\begin{pmatrix} R \\ L \end{pmatrix} = O \begin{pmatrix} \psi_1 \\ \psi_2 \end{pmatrix} \quad (3.2)$$

It is then possible to consider the left and right travelling transmission:

$$\begin{pmatrix} R_{\text{out}} \\ L_{\text{out}} \end{pmatrix} = O^{-1} M O \begin{pmatrix} R_{\text{in}} \\ L_{\text{in}} \end{pmatrix} \quad (3.3)$$

Where  $O^{-1} M O$  is known as the  $ABCD$  matrix, defined as:

$$O^{-1} M O = \begin{pmatrix} A & B \\ C & D \end{pmatrix} \quad (3.4)$$

By expanding the equations for inward and outward travelling waves, the matrices for transmission and reflection can be obtained:

$$T = A - B D^{-1} C \quad (3.5)$$



$$\tilde{T} = D^{-1} \quad (3.6)$$

$$R = BD^{-1}C \quad (3.7)$$

$$\tilde{R} = -D^{-1}C \quad (3.8)$$

Where  $T$  and  $R$  define the transmission and reflection in the forward-travelling case, and  $\tilde{T}$  and  $\tilde{R}$  define the transmission and reflection in the backward-travelling case.

These matrices are calculated for each slice and the net matrices are updated. The transmission values themselves are then obtained by using Singular Value Decomposition on these matrices. The net conductance is simply the sum of the transmission values.

### 3.2.1 Generation of $M$ matrix

The specific equations solved to obtain the transmission matrices are produced as follows.

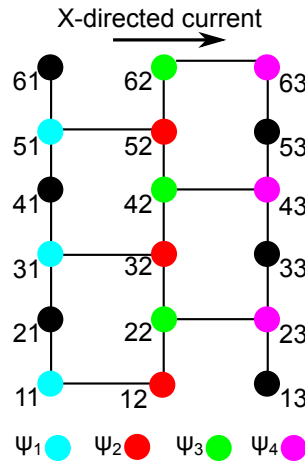


FIGURE 3.2: A diagram of an example lattice to how the simultaneous equations are constructed, in this case demonstrating the case of X-directed current. The different groups of sites are marked in different colours.

Firstly the equivalent sites are put in to vectors, so the equations can be combined in a linear algebra expression. In the example diagram in Figure 3.2, the vectors are defined as:

$$\psi_1 = \begin{pmatrix} \psi_{11} \\ \psi_{31} \\ \psi_{51} \end{pmatrix}, \quad \psi_2 = \begin{pmatrix} \psi_{12} \\ \psi_{32} \\ \psi_{52} \end{pmatrix}, \quad \psi_3 = \begin{pmatrix} \psi_{22} \\ \psi_{42} \\ \psi_{62} \end{pmatrix}, \quad \psi_4 = \begin{pmatrix} \psi_{23} \\ \psi_{43} \\ \psi_{63} \end{pmatrix} \quad (3.9)$$

Applying the TISE (Equation (2.4)) to this system obtains the following equations:

$$E_2\psi_2 = N_3\psi_3 + \psi_1 \quad (3.10)$$

$$E_3\psi_3 = N_2\psi_2 + \psi_4 \quad (3.11)$$

Where  $E_2$  and  $E_3$  are the  $(E - V)$  vectors (i.e. the energy minus the site potential) for the sites in the  $\psi_2$  and  $\psi_3$  vectors respectively, and  $N_2$  and  $N_3$  are matrices which define the links between the sites, in this case defined as:

$$N_3 = \begin{pmatrix} 1 & 0 & 0 \\ 1 & 1 & 0 \\ 0 & 1 & 1 \end{pmatrix}, \quad N_2 = \begin{pmatrix} 1 & 1 & 0 \\ 0 & 1 & 1 \\ 0 & 0 & 1 \end{pmatrix} \quad (3.12)$$

Enabling wrapping simply adds wrapped links in the X direction, making the appropriate changes to the  $N_{\{2,3\}}$  matrices. However note that to use X-wrapping, the sample size in the X direction must be a multiple of 2 in order to obtain a physical system. This check is present in our program.

Solving these equations for the transfer matrix,  $M$ , obtains the following block matrix:

$$M = \begin{pmatrix} -N_3^{-1} & E_2N_3^{-1} \\ -E_3N_3^{-1} & E_2E_3N_3^{-1} - N_2 \end{pmatrix} \quad (3.13)$$

It is this matrix which is produced and used in Equation (3.4) to calculate the transmission matrices.

In the case without magnetic field, the  $O$  matrix is simply defined by the block matrix:

$$O = \frac{1}{\sqrt{2}} \begin{pmatrix} 1 & 1 \\ i & -i \end{pmatrix} \quad (3.14)$$

This can be derived by consideration of the probability current.

### 3.2.2 Updating transmission matrices

The equations used to update the net  $T$ ,  $R$ ,  $\tilde{T}$  and  $\tilde{R}$  matrices can be derived by considering transmission (and reflection) through two blocks, as shown in Figure 3.3 in the case of transmission.

Including the contribution from each possible path results in a geometric sum, obtaining the following equations:

$$T_{\text{net}} = T_2 \left( 1 - \tilde{R}_1 R_2 \right) T_1 \quad (3.15)$$

$$\tilde{T}_{\text{net}} = \tilde{T}_1 \left( 1 - R_2 \tilde{R}_1 \right) \tilde{T}_2 \quad (3.16)$$

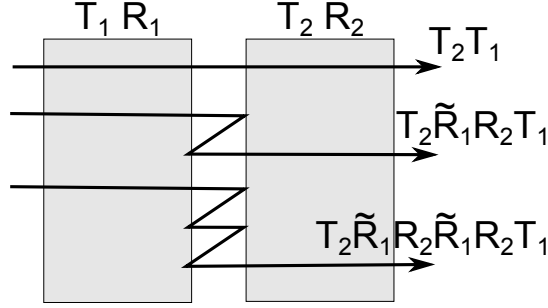


FIGURE 3.3: A diagram showing the net transmission across two blocks. One must include the contributions from all of the possible paths, resulting in a geometric sum.

$$R_{\text{net}} = R_1 + \tilde{T}_1 \left( 1 - R_2 \tilde{R}_1 \right)^{-1} R_2 T_1 \quad (3.17)$$

$$\tilde{R}_{\text{net}} = \tilde{R}_2 + T_2 \left( 1 - \tilde{R}_1 R_2 \right)^{-1} \tilde{R}_1 \tilde{T}_2 \quad (3.18)$$

It is these equations which are used to update the net transmission matrices.

### 3.3 Tests of correctness

#### 3.3.1 Unitarity checking

The first test, built in to the software, is calculating the unitarity of the net transmission matrices, checking that the following condition holds:

$$\begin{pmatrix} T & \tilde{R} \\ R & \tilde{T} \end{pmatrix}^\dagger \begin{pmatrix} T & \tilde{R} \\ R & \tilde{T} \end{pmatrix} = I \quad (3.19)$$

The Frobenius norm (square root of the squared sums) of the off-diagonal elements is calculated, and checked to be close to zero (values less than  $10^{-6}$  were considered acceptable). For efficiency reasons this check is actually implemented in terms of the transmission matrices themselves. The following conditions are checked, and the results are combined.

$$T^\dagger T + R^\dagger R = 1 \quad (3.20)$$

$$\tilde{T}^\dagger \tilde{T} + \tilde{R}^\dagger \tilde{R} = 1 \quad (3.21)$$

$$T^\dagger \tilde{R} + R^\dagger \tilde{T} = 0 \quad (3.22)$$

This provides a quick check that the linear algebra calculations are behaving as expected, but it does not prove that the results are physical in itself. To this end, we also tested results against analytical equations which we produced.

### 3.3.2 Analytical tests

By considering the net matrix across a pure sample, it is possible to obtain an analytical solution for the transmission values (and so conductance). This is done by writing the recurrence relations as a finite difference equation.

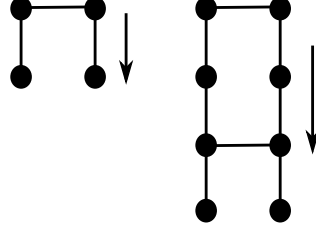


FIGURE 3.4: A diagram of the “ladder” configuration for which the analytical tests were derived.

For example, in the case of Y-directed conduction down a vertical “ladder” (i.e. where the horizontal length is 2), one can define two transfer matrices (calculated as explained in Section 3.2.1) for odd (no horizontal link) and even (linked) steps (note that in the case of x-wrapping these would simply be equal to one another).

$$M_{\text{even}} = \begin{pmatrix} 0 & 0 & 1 & 0 \\ 0 & 0 & 0 & 1 \\ -1 & 0 & E & 0 \\ 0 & -1 & 0 & E \end{pmatrix}, \quad M_{\text{odd}} = \begin{pmatrix} 0 & 0 & 1 & 0 \\ 0 & 0 & 0 & 1 \\ -1 & 0 & E & -1 \\ 0 & -1 & -1 & E \end{pmatrix} \quad (3.23)$$

For one step down the sample, one obtains:

$$M_{\text{even}}M_{\text{odd}} = \begin{pmatrix} -1 & 0 & E & -1 \\ 0 & -1 & -1 & E \\ -E & 0 & E^2 - 1 & -E \\ 0 & -E & -E & E^2 - 1 \end{pmatrix} = \begin{pmatrix} a_n & b_n \\ c_n & d_n \end{pmatrix} \quad (3.24)$$

$M_{\text{even}}$  and  $M_{\text{odd}}$  can also be written in terms of block matrices:

$$M_{\text{even}} = \begin{pmatrix} 0 & 1 \\ -1 & E \end{pmatrix}, \quad M_{\text{odd}} = \begin{pmatrix} 0 & 1 \\ -1 & \lambda \end{pmatrix} \quad (3.25)$$

Where  $\lambda = E \pm 1$  (note in the case of X-wrapping then  $\lambda = E$ ). Considering pairs of steps one obtains the following block matrices for the initial and second steps.

$$M = \begin{pmatrix} -1 & \lambda \\ -E & E\lambda - 1 \end{pmatrix}, \quad M^2 = \begin{pmatrix} 1 - E\lambda & \lambda(E\lambda - 1) - \lambda \\ E - E(E\lambda - 1) & (E\lambda - 1)^2 - E\lambda \end{pmatrix} \quad (3.26)$$

The eigenvalues of  $M$  are:

$$\xi = \frac{1}{2} \left( E\lambda - 2 - \sqrt{E^2\lambda^2 - 4E\lambda} \right) \quad (3.27)$$

$$\frac{1}{\xi} = \frac{1}{2} \left( E\lambda - 2 + \sqrt{E^2\lambda^2 - 4E\lambda} \right) \quad (3.28)$$

It is now possible to solve the following recursion relations to obtain the coefficients for the general recurrence relation, since the matrix elements can be expressed as a combination of the initial eigenvalues:

$$\alpha_1 + \alpha_2 = 1 \quad \alpha_1\xi + \frac{\alpha_2}{\xi} = -1 \quad (3.29)$$

$$\beta_1 + \beta_2 = 1 \quad \beta_1\xi + \frac{\beta_2}{\xi} = \lambda \quad (3.30)$$

$$\gamma_1 + \gamma_2 = 0 \quad \gamma_1\xi + \frac{\gamma_2}{\xi} = -E \quad (3.31)$$

$$\delta_1 + \delta_2 = 1 \quad \delta_1\xi + \frac{\delta_2}{\xi} = E\lambda - 1 \quad (3.32)$$

Solving these simultaneous equations for the coefficients (in Greek letters) results in the following equations for the submatrix blocks:

$$a_n = \left( 1 - \frac{-(1+\xi)}{\frac{1}{\xi} - 1} \right) \xi^n + \frac{-(1+\xi)}{\xi^n \left( \frac{1}{\xi} - 1 \right)} \quad (3.33)$$

$$b_n = \frac{\lambda\xi^n}{\xi - \frac{1}{\xi}} - \frac{\lambda}{\xi^n \left( \xi - \frac{1}{\xi} \right)} \quad (3.34)$$

$$c_n = \frac{-E\xi^n}{\xi - \frac{1}{\xi}} + \frac{E}{\xi^n \left( \xi - \frac{1}{\xi} \right)} \quad (3.35)$$

$$d_n = \left( \frac{E\lambda - 1 - \frac{1}{\xi}}{\xi - \frac{1}{\xi}} \right) \xi^n + \left( 1 - \left( \frac{E\lambda - 1 - \frac{1}{\xi}}{\xi - \frac{1}{\xi}} \right) \right) \frac{1}{\xi^n} \quad (3.36)$$

Calculating the general form of  $O^{-1}MO$  obtains the following equations for the transmission and reflection values:

$$T = \frac{2}{(a+d) + (c-b)i} = \tilde{T} \quad (3.37)$$

$$R = \frac{(a-d) + (b+c)i}{(a+d) + (c-b)i} \quad (3.38)$$

$$\tilde{R} = \frac{(a-d) - (b+c)i}{(a+d) + (c-b)i} \quad (3.39)$$

Equation (3.37) is used to calculate the transmission values. Substituting in the relations and simplifying the results obtains the following equations:

In the case of real  $\xi$ :

$$T = \frac{2}{(\xi^n + \xi^{-n}) + \frac{-E-\lambda}{\xi-\xi^{-1}} (\xi^n - \xi^{-n}) i} \quad (3.40)$$

Where  $\xi$  is defined by:

$$\xi = \frac{E\lambda}{2} - 1 - \sqrt{\frac{E^2\lambda^2}{4} - E\lambda} \quad (3.41)$$

Note that since  $\lambda = E \pm 1$ ,  $\xi$  can be both real and complex. In the case of complex  $\xi$ :

$$T = \frac{2}{2 \cos(n\phi) + \frac{-E-\lambda}{\sin(\phi)} (\xi^n - \xi^{-n}) i} \quad (3.42)$$

With the following definitions for  $\phi$ :

$$\cos(\phi) = \frac{E\lambda}{2} - 1 \quad , \quad \sin(\phi) = -\sqrt{E\lambda - \frac{E^2\lambda^2}{4}} \quad (3.43)$$

A plot of the results from these analytical equations and the program output is shown in Figure 3.5 for the 2×4 ladder. The program output and analytical results matched, and this was also tested for various lengths of ladders. The source code for this program is given in Appendix B.1. The same check was also repeated for a horizontal chain with X-directed current.

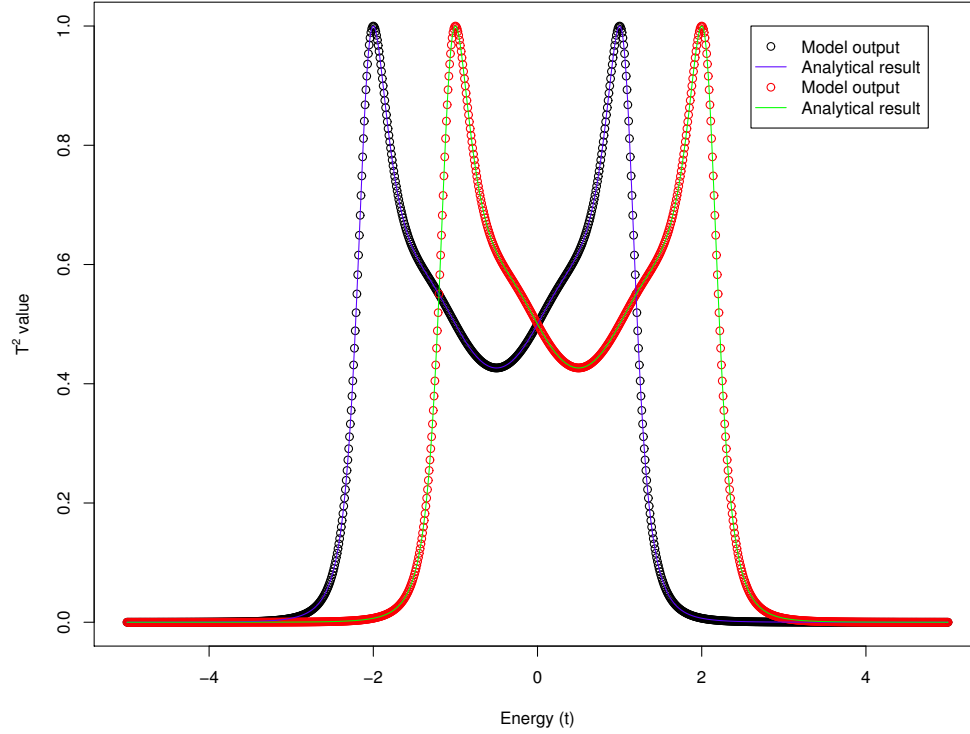


FIGURE 3.5: A plot of the results of the analytical equations against the program output for a  $2 \times 4$  lattice, with conduction in the Y-direction as shown in Figure 3.4. The squares of the transmission values are plotted against the energy. The circles are the program output, and the lines are the analytical results. Note there are two T values since the (horizontal) width is 2. The net conductance is simply the sum of the transmission values.

### 3.4 Implementation of magnetic field

The addition of magnetic field introduces a phase factor in to the  $N_{\{2,3\}}$  matrices described in Subsection 3.2.1.

So, in the case of the magnetic vector potential being directed in the Y-direction, and so varying in the X-direction the 1's in the matrices must be replaced by a phase factor  $e^{\pm i\phi x_n}$  where  $\phi$  is the magnetic flux and  $x_n$  is the column number of the lattice site.

The addition of magnetic field also requires that the  $O$  matrix is modified in the case where the current and magnetic vector potential are directed in the same direction. For efficiency reasons the  $O$  matrix was split up and defined in terms of a  $u$  submatrix, as follows:

$$O = \frac{1}{\sqrt{2}} \begin{pmatrix} 1 & 1 \\ u & -u \end{pmatrix} \quad (3.44)$$

Where  $u = i$  in the case of no magnetic field.

In this case,  $u$  must take in to account the phase factor, so if Y-directed magnetic vector potential is applied to the ladder example in Subsection 3.3.2 then:

$$u = \begin{pmatrix} ie^{i\phi} & 0 \\ 0 & ie^{2i\phi} \end{pmatrix} \quad (3.45)$$

Note that to convert from the flux to the magnetic field, we must consider the area of the hexagons, resulting in the following equation:

$$B = \frac{4\phi}{3\sqrt{3}} \quad (3.46)$$

The implementation of magnetic field can be tested by checking the existence and positions of Quantum Hall plateaus in a clean sample. The theoretical positions of the Quantum Hall steps can be predicted by substituting the relation for magnetic field in Equation (3.46) in to Equation (2.30), resulting in the following equation:

$$E_N = \pm 3 \sqrt{\frac{2\phi N}{3\sqrt{3}}} \quad (3.47)$$

The Quantum Hall steps from the program data for a clean sample, along with the theoretical positions predicted by Equation (3.47) are show in Figure 3.6.



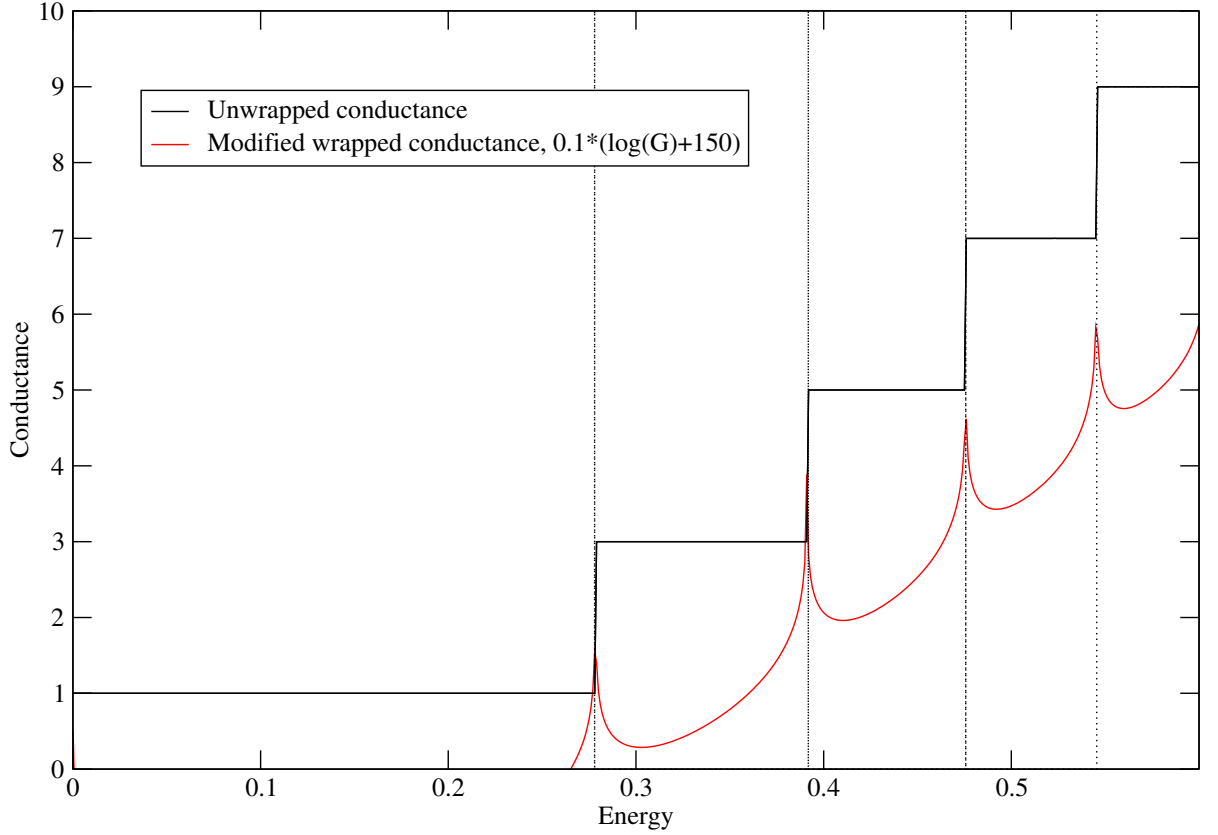


FIGURE 3.6: A plot of the quantum Hall steps in the wrapped and unwrapped conductance for a  $160 \times 277$  sample, with the current in the X-direction and magnetic vector potential in the Y-direction, at a flux of 0.0227. The wrapped conductance is appropriately modified so it can be viewed on the same scale. The theoretical values of the QHE steps are shown with dotted lines.

### 3.5 Implementation of disorder

Disorder is implemented by simulating electronic vacancies on the lattice sites, which could be created experimentally, through the addition of adatoms such as Hydrogen, which bond to the sites. The vacancies themselves are implemented by setting the on-site lattice potential,  $U_0$  to a high, finite value (in our results  $U_0 = 1000$  was used).

A Monte Carlo approach is used to calculate the results for specified disorder concentrations on the A and B sublattices. This means that the lattice is repeatedly generated with randomised positions of vacancies and the results are averaged across all randomly generated lattices.

To achieve this the random number generator **ran2** from *Numerical Recipes in Fortran 77* [23] was used. A fixed number of vacancies is then calculated from the given vacancy concentration and lattice size. Random sites are then chosen and, if all the vacancies for

that sublattice have not yet been allocated, made in to a vacancy. If they are already a vacancy then they are skipped and a new random site is generated. The source code for this is given in Appendix B.2. The standard error of the repeated randomised samples is also calculated to provide an indication of the reliability of the results. It was found that 50 repeats gave a good trade-off between computation time and reliability.

## Chapter 4

# Results

This chapter covers the main results from the data which we have produced from the program. Square lattices were used in order to ensure there are no effects from 1-dimensional effects. X-directed current and Y-directed magnetic vector potential were used, as this is slightly more efficient, since in the case of the X-directed current the matrices only have a rank of  $\frac{LIMY}{2}$ , and having them directed in different directions means that the  $u$  matrix does not have to be modified for magnetic field (see Section 3.4).

## 4.1 Size effects

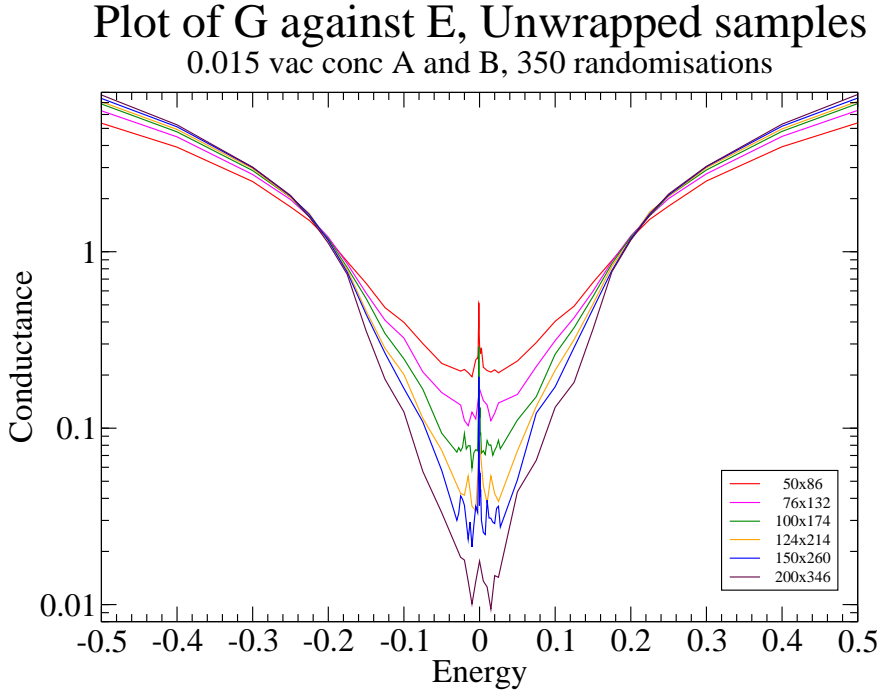


FIGURE 4.1: Conductance for various sizes of square samples, showing the transition from the delocalised to the localised regime near  $E = \pm 0.2$

In order to observe the effect of sample size on conductance, the net conductance for differently sized square samples was calculated, at 1.5% vacancy concentration on the A and B sublattices with 350 randomisations.

Figure 4.1 shows that at energies greater than  $\pm 0.2$  all states are delocalised, since the conductance converges to the same values at all sample sizes. Note that the conductance decreases with size in the localised regime due to the exponential dependence of conductance on sample size in this regime (see Equation (2.32)). A peak in the conductance is visible near zero energy, this was investigated in more detail, as shown in Section 4.2.

## 4.2 Zero energy conductance peak

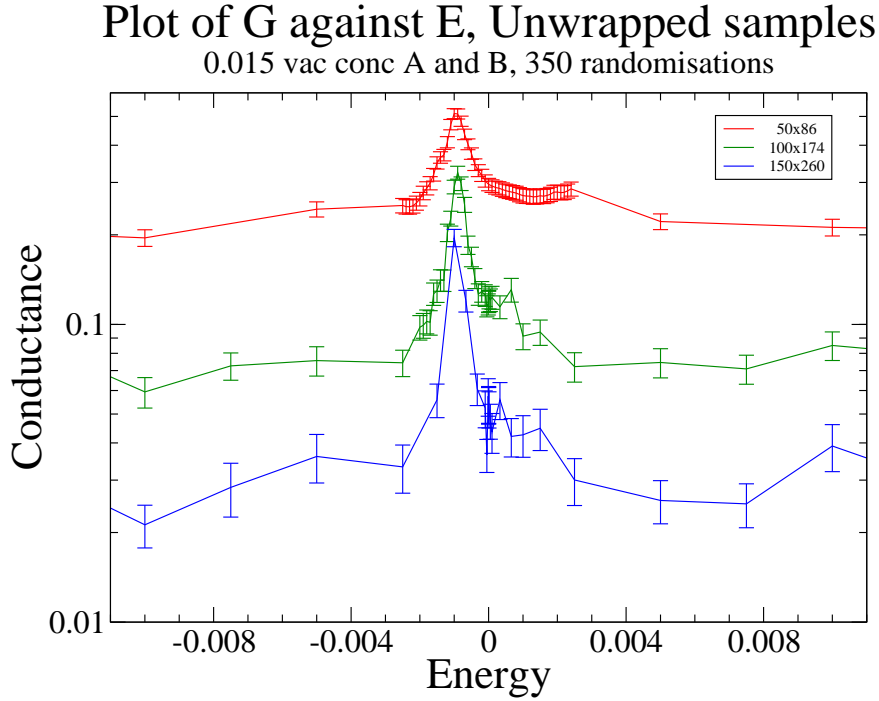


FIGURE 4.2: A zoomed plot of the central, low energy region of Figure 4.1 showing the conductance peak at  $E = -10^{-3}$ .

The zero-energy peak visible in Figure 4.1 was investigated in more detail at a much higher energy resolution. The resolution was lowered for the larger sample sizes due to the increase in necessary computation time.

Figure 4.2 shows direct evidence for delocalised states close to zero energy. Note that the fact that the peak is not centred on zero energy is a result of the finite on-site potential used in simulating the vacancies. This results in an energy shift of the reciprocal of the energy gap, and so the peak appears at an energy of  $-10^{-3}$ . The localisation length of these states has been found to be limited by the sample size, due to the finite sizes used in the model.

### 4.3 Localisation length

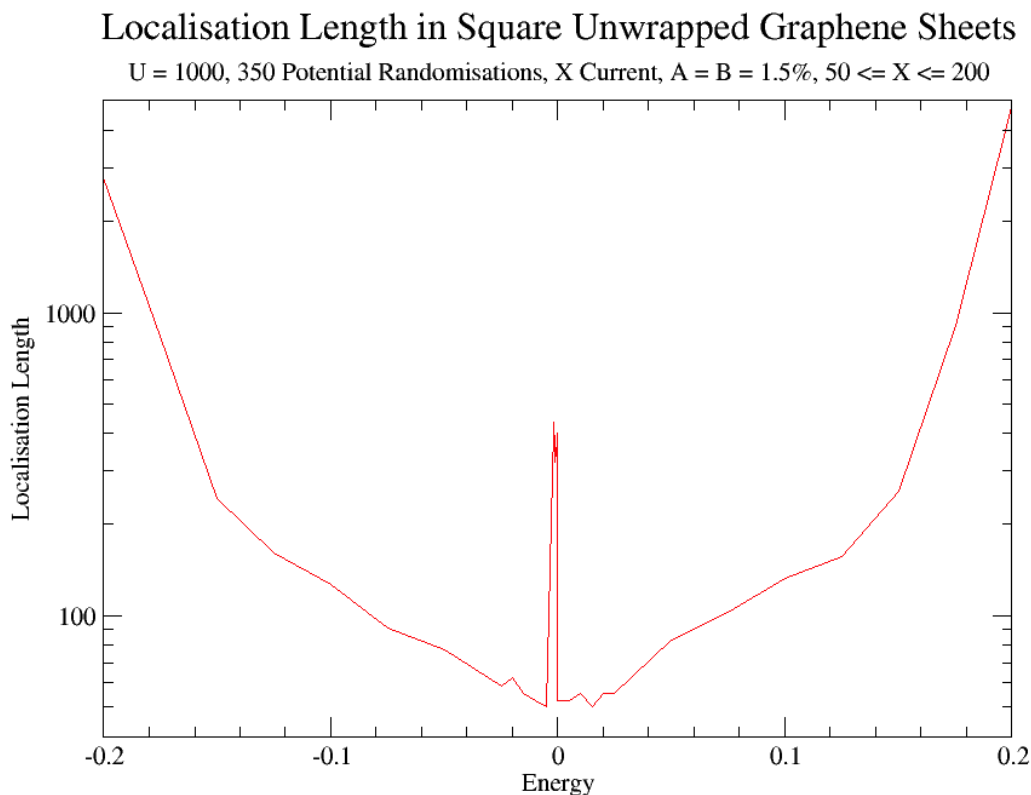


FIGURE 4.3: A plot of the localisation length against energy.

The localisation length was calculated by producing results for square samples of various widths (square samples, varying the horizontal size between 50 and 200). Then plotting the logarithm of the conductance and fitting the gradient to obtain the localisation length,  $\xi$  (see Equation (2.32) in Section 2.8).

Figure 4.3 shows there is a significant peak in the localisation length near zero energy. Our sample sizes increased to approximately 200 at maximum, in each direction, so any localisation length above this is sample limited, and so the states are effectively delocalised. This shows that the peak in conductance at zero energy appears to be from delocalised states.

## 4.4 Phase diagrams

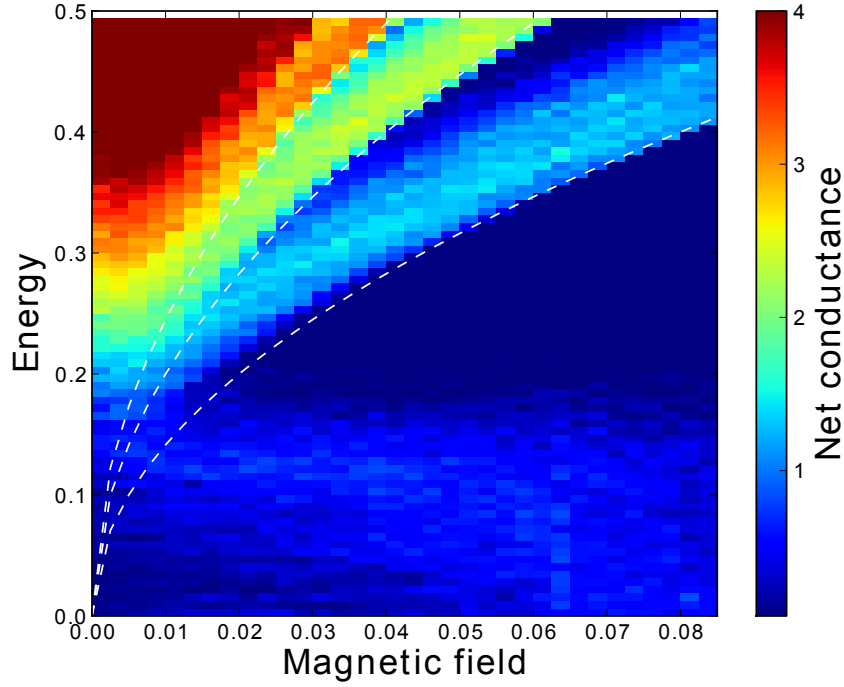


FIGURE 4.4: Wrapped sample with the theoretical position of the 1st, 2nd and 3rd Landau level plotted in the dashed white lines, see Equation (2.30). The sample size was  $100 \times 174$ , with X wrapping enabled, 1.5% vacancy concentration on the A and B sublattices and 20 randomisations.

In order to observe the effect of magnetic field on the conductance, the conductance was calculated over a range of energy and magnetic field values. Figure 4.4 was calculated for 20 randomisations with 1.5% vacancy concentration on the A and B sublattices for a  $100 \times 74$  sample.

Figure 4.4 shows close agreement with the theory at high magnetic field. At low fields the phase diagram shows the transition between localised and delocalised states. Since this transition must be continuous the energy levels “float” up as the magnetic field tends to zero[24], a phenomenon which was first described by Khmel'nitskii[1] and Laughlin[25]. This is visible in Figure 4.4 for magnetic fields below 0.01.

The area of low energy conductance was investigated in more detail, as shown in Figure 4.5.

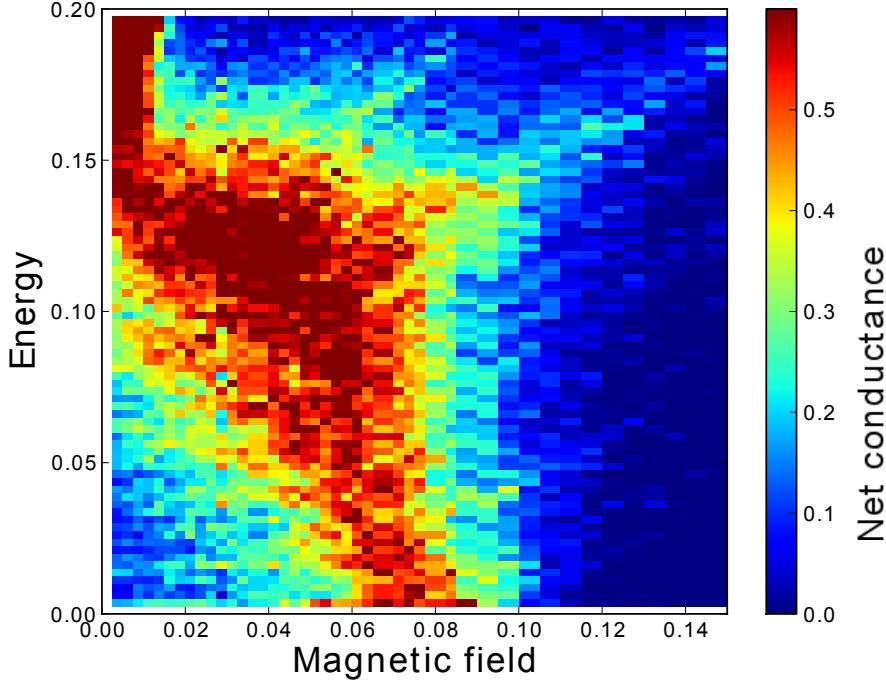


FIGURE 4.5: A zoom of Figure 4.4 at low energy, showing delocalised states produced by the applied magnetic field. The sample size was  $100 \times 174$ , with X wrapping enabled, 1.5% vacancy concentration on the A and B sublattices and 50 randomisations.

Figure 4.5 shows the behaviour of the zeroth Landau level, which is suggestive of delocalised states at low energies, produced by the applied magnetic field.

At very low energy we observe localisation until a critical field is reached, whereby the magnetic field destroys the quantum interference responsible for the localisation. While at strong magnetic fields this delocalised regime is lost, and the states are localised due to the small cyclotron orbits of the electrons.

## 4.5 Comparison with current experimental capabilities

Our results do not use standard units, the energy is in terms of the hopping integral,  $t \approx 2.8\text{eV}$ [11], and the magnetic field is in terms of the magnetic flux through one hexagon in the lattice. This was done to simplify the equations and obviate the need to remember constants in the programming. These units can be converted to standard units by considering the area of the hexagon in the lattice in the case of the magnetic field, and substituting for the hopping integral in the case of the energy.



In our units an energy of 0.2 corresponds to approximately 600meV, whilst a magnetic field of 0.1 corresponds to approximately 100 Tesla. For comparison, the current maximum achievable energy in experiment is approximately 100meV, and for magnetic field is approximately 10 Tesla.

Clearly the scale we have used is currently unachievable in experiment. However, the model can be used with realistic energies and fields, but this would require increasing the lattice size significantly too (to reflect what would be used experimentally), this comes at a great cost of computational time and is intractable with the current implementation and resources. Instead, we increased the disorder concentration so that the smaller scale of the lattice still allows for observable results.



## Chapter 5

# Conclusion

### 5.1 Summary

In summary, a numerical model of electron transport in doped, monolayer graphene was produced. The model was written in FORTRAN 77 and uses the tight binding approximation and scattering matrix approach to calculate the net conductance through graphene samples of variable size, applied magnetic field and disorder. The model was tested against analytical test cases and known results to ensure correctness.

We produced results for square lattices of varying sizes to investigate size effects, and calculated the effective localisation length of the electron wavefunctions. Of particular interest is the peak near zero energy which appears to result from delocalised states produced by the disorder.

Phase diagrams were produced and the Landau levels matched expectation from the theory of pure samples, but with the addition of the floating described by Khmelnitskii[1]. The zeroth Landau level was also visible, and shows the existence of a critical magnetic field for conduction at zero energy, and the presence of delocalised states in this region, which is destroyed at high magnetic fields.

### 5.2 Future work

There are still many areas for future work in the project and the broader context of the effects of doping in graphene.

One could investigate the effect of approximating the vacancies with a finite on-site potential. This is the origin of the offset (from zero energy) of the central peak in Figure 4.2. This could be done by repeating the calculations for different values of  $U_0$  to see how

this affects the results, and where the best trade-off between computational accuracy and physicality is to be found.

The effect of lattice size and disorder concentration on the net conductance could also be investigated. The expected scaling with  $N_0$ , the impurity concentration, is  $E \propto \sqrt{N_0}$  and  $B \propto N_0$  [26].

A larger investigation could attempt to implement many-body physics. The model presented here is a single electron system, where electron-electron interactions are neglected, and the tight binding approximation means that electrons may only hop to nearest neighbour sites. A more physical description is provided by the variable range hopping model, where the probability of hopping between sites depends upon their spatial separation and energy separation[20].

# Appendix A

## Flowchart

**driver.f:** Sets initial conditions

- Lattice size: LIMX, LIMY
- Energy range: EMIN, EMAX, NE
- Direction of current traversal: CURRENT
- Magnetic Flux: FLUX
- Direction of Magnetic Vector Potential: GAUGE
- Impurity potential: U
- *Impurity concentrations*

**vacancy.f:** Allocates randomised vacancy sites in lattice.

**GENVACFIX(V, LIMX, LIMY, U, ALAT, BLAT, SEED):** Generates a fixed number of vacancies, with vacancy concentration ALAT and BLAT on the A and B sublattices respectively, and the vacancy potential U.

*Other functions omitted for brevity.*

**tmatrix.f:** Only contains GETTRANS()

**GETTRANS(CURRENT, GAUGE, TVALS, NVALS, LIMX, LIMY, V, E, FLUX, WRAPX):** Calls appropriate GETTRANS function depending on the current direction and gauge chosen. Checks conditions on sample size.

**tmatrix{x,y}.f:** Handles calculations for {X,Y}-directed current

**GETTRANS{X,Y}(GAUGE, TVALS, LIMX, {LIMY, LIMY/2}, V, E, FLUX):** Main function which (through calling other functions) results in the calculation of the T values for the sample for {X,Y}-directed current.

**FILLU{X,Y}Y(U, FLUX, LIMX):** Fills the U matrix for {X,Y}-current, Y-gauge.

**FILLU{X,Y}X(U, FLUX, LIMX):** Fills the U matrix for {X,Y}-current, X-gauge.

**CALCMULT{X,Y}X(E, FLUX, POS, MULT, LIMX, {LIMY, LIMY/2}, V):** Calculates the transfer matrix of the current block for X-directed flux.

**CALCMULT{X,Y}Y(E, FLUX, POS, MULT, LIMX, {LIMY, LIMY/2}, V):** Calculates the transfer matrix of the current block for Y-directed flux.

*Specific functions called depend on choice of X-directed or Y-directed current.*

**trupdate.f:** Calculates T and R values for current transfer matrix, and updates net sample values.

**GENABCD(MULT, U, A, B, C, D, N):** Fills A, B, C and D submatrices, for square submatrix size N. Implemented for optimisation purposes.

**GENTANDRINC(A, B, C, D, TINC, RINC, TTILDEINC, RTILDEINC, N):** Performs linear algebra to obtain transmission/reflection coefficient submatrices from the transfer matrix for the current block.

**UPDATETANDR(T, R, TTILDE, RTILDE, TINC, RINC, TTILDEINC, RTILDEINC, N):** Updates the net transmission/reflection coefficient submatrices.

**linalg.f:** Contains many functions to simplify linear algebra calculations and LAPACK function calls.

**SQSVDVALS(MATRIX, OUTPUTS, N):** Carries out Singular Value Decomposition on the MATRIX and returns the values in OUTPUTS.

*Other functions omitted for brevity.*

**unitarity.f:** Contains three functions to test the unitarity of the transmission coefficient submatrices. This provides a good preliminary test for errors.

**CHECKUNI(T, R, TTILDE, RTILDE, N):** Calculates the unitarity of the net matrix (made up of the submatrices) through multiplication by the conjugate transpose of the matrix. Output should be approximately zero.

*Other functions omitted for brevity.*

**util.f:** Contains various functions for convenience, including for zeroing and printing matrices.

**CONDUCTANCE (TVALS, LIMX):** Calculates the conductance (returned as a double) from the passed TVALS, by summing the square of the TVALS.

*Other functions omitted for brevity.*

# Appendix B

## Source code excerpts

This appendix contains brief, important code excerpts. Note that all of the source code is available on Github[22].

### B.1 Analytical ladder test program

Source code for the analytical test of the ladder case described in Subsection 3.3.2. This code is also available on the Github repository[22].

analyticalsimple.f

---

```
PROGRAM PLOTNOWRAP
IMPLICIT NONE
DOUBLE PRECISION E/-5.0/, LAMBDA, TP, TN, SINP, COSP, PHI, SQRTARG
+      , REALXI
INTEGER F/1/, N/1/
CHARACTER*3 VALUE

c$$$ Set N to command line argument
CALL GETARG(1, VALUE)
READ(UNIT=VALUE, FMT=*) N

DO F = 1, 2002
c$$$ Check if xi complex or real
c$$$ use appropriate case to calculate T
c$$$ repeat with other transmission value
c$$$ increment E

      LAMBDA=E
      SQRTARG=((((E**2)*(LAMBDA**2))/4.0) - (E*LAMBDA))
      IF (SQRTARG .GE. 0) THEN
        REALXI=((E*LAMBDA)/2.0) - SQRT(SQRTARG) - 1.0
        TP=4*((REALXI**N + REALXI**(-1.0*N))**2 + ((E+LAMBDA)/(
+          REALXI-(REALXI**(-1.0)))*(REALXI**N - REALXI**(-1.0*N
+          ))**2)/((REALXI**N + REALXI**(-1.0*N))**2 + ((E+
+          LAMBDA)/(REALXI-(REALXI**(-1.0)))*(REALXI**N - REALXI**
```

---

```

+          (-1.0*N))))**2)**2
      ELSE
        SINP=-1.0*SQRT((E*LAMBDA) - ((E**2 * LAMBDA**2)/4.0))
        COSP=((E*LAMBDA)/2.0) -1.0
        PHI=ATAN2(SINP, COSP)
        TP=4*(((2*COS(N*PHI))**2) + (((-E-LAMBDA)/(SIN(PHI))))
+          *SIN(N*PHI))**2) / (((4*(COS(N*PHI)**2)) + (((-E-LAMBDA
+          )/SIN(PHI))*SIN(N*PHI))**2)**2)
      ENDIF

      LAMBDA=E
      SQRTARG=(((E**2)*(LAMBDA**2))/4.0) - (E*LAMBDA))
      IF (SQRTARG .GE. 0) THEN
        REALXI=((E*LAMBDA)/2.0) - SQRT(SQRTARG) - 1.0
        TN=4*((REALXI**N + REALXI**(-1.0*N))**2 + (((E+LAMBDA)/(
+          REALXI-(REALXI**(-1.0))))*(REALXI**N - REALXI**(-1.0*N
+          ))**2)/((REALXI**N + REALXI**(-1.0*N))**2 + (((E+
+          LAMBDA)/(REALXI-(REALXI**(-1.0))))*(REALXI**N - REALXI**
+          (-1.0*N))))**2)**2
      ELSE
        SINP=-1.0*SQRT((E*LAMBDA) - ((E**2 * LAMBDA**2)/4.0))
        COSP=((E*LAMBDA)/2.0) -1.0
        PHI=ATAN2(SINP, COSP)
        TN=4*(((2*COS(N*PHI))**2) + ((((-E-LAMBDA)/(SIN(PHI))) *
+          SIN(N*PHI))**2)) / ((4*(((COS(N*PHI)**2)) + (((-E-LAMBDA
+          )/SIN(PHI))*SIN(N*PHI))**2)**2)
      ENDIF

      WRITE (*,10) E,TP+TN

      E=E+0.005
    END DO

10  FORMAT (3E15.5E4)
    END

```

---

## B.2 Allocation of random vacancy sites

This is the subroutine used to allocate the vacancy sites in the lattice mentioned in Section 3.5, using the `ran2` random number generator from *Numerical Recipes in Fortran 77* [23]. This code is also available on the Github repository[22].

`vacancy.f`: SUBROUTINE GENVACFIX

---

```

C      Subroutine to apply fixed number of sites to A and B
      SUBROUTINE GENVACFIX(V, LIMX, LIMY, U, ALAT, BLAT, SEED)
      IMPLICIT NONE

      INTEGER LIMX, LIMY
      DOUBLE PRECISION V(LIMX,LIMY), U, ALAT, BLAT
      REAL GETRAND
      REAL RANDOM
      LOGICAL KEEPGOING/.TRUE./
      INTEGER NALAT/0/, NBLAT/0/, XC, YC, SEED

```



---

```

    INTEGER CURALAT/0/, CURBLAT/0/
    DOUBLE PRECISION, PARAMETER :: ZERO = 0.0

    KEEPGOING=.TRUE.
    CURALAT=0
    CURBLAT=0

    NALAT=NINT(ALAT*LIMX*LIMY*0.5)
    NBLAT=NINT(BLAT*LIMX*LIMY*0.5)
    CALL DLASET('ALL', LIMX, LIMY, ZERO, ZERO, V, LIMX)

    IF ((CURALAT.EQ.NALAT) .AND. (CURBLAT.EQ.NBLAT)) THEN
        KEEPGOING = .FALSE.
    ENDIF

    DO WHILE (KEEPGOING .EQV. .TRUE.)
        RANDOM=GETRAND(SEED)
        XC=INT((RANDOM*LIMX)+1)
        RANDOM=GETRAND(SEED)
        YC=INT((RANDOM*LIMY)+1)

C      IF SUBLATTICE A
        IF (V(XC,YC).NE.U) THEN
            IF (MOD(XC,2).EQ. MOD(YC,2)) THEN
                IF (CURALAT .LT. NALAT) THEN
                    V(XC,YC) = U
                    CURALAT=CURALAT+1
                ENDIF
            ELSE
                IF (CURBLAT .LT. NBLAT) THEN
                    V(XC,YC) = U
                    CURBLAT=CURBLAT+1
                ENDIF
            ENDIF
        ENDIF

        IF ((CURALAT.EQ.NALAT) .AND. (CURBLAT.EQ.NBLAT)) THEN
            KEEPGOING = .FALSE.
        ENDIF
    ENDDO

    RETURN
END

```

---



# Bibliography

- [1] D. E. Khmel'nitskii. *Phys. Lett.*, 106A:182, 1984.
- [2] KS Novoselov, AK Geim, SV Morozov, D. Jiang, Y. Zhang, SV Dubonos, IV Grigorieva, and AA Firsov. Electric field effect in atomically thin carbon films. *Science*, 306(5696):666, 2004.
- [3] A.K. Geim and A.H. MacDonald. Graphene: Exploring carbon flatland. *Physics Today*, 60(8):35, 2007.
- [4] Alexander N. Obraztsov. Chemical vapour deposition: Making graphene on a large scale. *Nat Nano*, 4(4):212–213, 2009.
- [5] M. I. Katsnelson, K. S. Novoselov, and A. K. Geim. Chiral tunnelling and the klein paradox in graphene. *Nat Phys*, 2(9):620–625, 2006.
- [6] A.K. Geim and K.S. Novoselov. The rise of graphene. *Nature materials*, 6(3):183–191, 2007.
- [7] K. Jensen, K. Kim, and A. Zettl. An atomic-resolution nanomechanical mass sensor. *Nat Nano*, 3(9):533–537, 2008.
- [8] Fengnian Xia, Thomas Mueller, Yu-ming Lin, Alberto Valdes-Garcia, and Phaedon Avouris. Ultrafast graphene photodetector. *Nat Nano*, 4(12):839–843, 2009.
- [9] Yanqing Wu, Yuming Lin, Ageeth A. Bol, Keith A. Jenkins, Fengnian Xia, Damon B. Farmer, Yu Zhu, and Phaedon Avouris. High-frequency, scaled graphene transistors on diamond-like carbon. *Nature*, 472(7341):74–78, 2011.
- [10] Fengnian Xia, Damon B. Farmer, Yuming Lin, and Phaedon Avouris. Graphene field-effect transistors with high on/off current ratio and large transport band gap at room temperature. *Nano Letters*, 10(2):715–718, 2010. PMID: 20092332.
- [11] A. Neto, F. Guinea, N. Peres, et al. The electronic properties of graphene. *Reviews of Modern Physics*, 81(1):109–162, 2009.
- [12] R. S. Deacon, K.-C. Chuang, R. J. Nicholas, K. S. Novoselov, and A. K. Geim. Cyclotron resonance study of the electron and hole velocity in graphene monolayers. *Phys. Rev. B*, 76:081406, Aug 2007.

- [13] Mikhail I. Katsnelson. *Graphene: Carbon in Two Dimensions*. Cambridge University Press, Cambridge, UK, 1992.
- [14] Andrea F. Young and Philip Kim. Quantum interference and klein tunnelling in graphene heterojunctions. *Nat Phys*, 5(3):222–226, 2009.
- [15] Yoseph Imry and Rolf Landauer. Conductance viewed as transmission. *Reviews of Modern Physics*, 71(2):306–312, 1999.
- [16] F Miao, S Wijeratne, Y Zhang, U C Coskun, W Bao, and C N Lau. Phase-coherent transport in graphene quantum billiards. *Science (New York, N.Y.)*, 317(5844):1530–3, September 2007.
- [17] D. R. Yennie. Integral quantum hall effect for nonspecialists. *Rev. Mod. Phys.*, 59:781–824, Jul 1987.
- [18] H. Paul. *Introduction to Quantum Theory*, pages 156–157. Cambridge University Press, Cambridge, UK, 2008.
- [19] S V Morozov, K S Novoselov, and A K Geim. Electron transport in graphene. *Physics-Uspekhi*, 51(7):744, 2008.
- [20] V. F. Gantmakher. *Electrons and Disorder in Solids*. Oxford University Press, Oxford, UK, 2005.
- [21] Patrick A. Lee and T. V. Ramakrishnan. Disordered electronic systems. *Rev. Mod. Phys.*, 57:287–337, Apr 1985.
- [22] James McMurray. Doping-effects-in-graphene repository, April 2013.
- [23] William H. Press, Saul A. Teukolsky, William T. Vetterling, and Brian P. Flannery. *Numerical Recipes in Fortran 77*, pages 272–273. Cambridge University Press, Cambridge, UK, 1992.
- [24] B.I. Halperin *et al.* Quantised hall conductance, current carrying edge states and the existence of extended states in a two-dimensional disordered potential. *Phys Rev B*, 25:2185–2190, 1982.
- [25] R. B. Laughlin. *Phys. Rev. Lett.*, 52:2304, 1984.
- [26] Steven E Martins, Freddie Withers, Marc Dubois, Monica F Craciun, and Saverio Russo. Tuning the transport gap of functionalized graphene via electron beam irradiation. *New Journal of Physics*, 15(3):033024, 2013.